

Shape fluctuations and radiation from thermally excited electronic states of boron clusters

T. Hóltzl*

*Furukawa Electric Institute of Technology, 1158 Budapest, Hungary
and ELKH-BME Computation Driven Chemistry Research Group and Department of Inorganic and Analytical Chemistry,
Budapest University of Technology and Economics, 1111 Budapest, Hungary*

P. Ferrari[‡] and E. Janssens[‡]

Quantum Solid-State Physics, Department of Physics and Astronomy, KU Leuven, 3001 Leuven, Belgium

K. Hansen[†]

*Lanzhou Center for Theoretical Physics, Key Laboratory of Theoretical Physics of Gansu Province,
Lanzhou University, Lanzhou, Gansu 730000, China
and Center for Joint Quantum Studies and Department of Physics, School of Science, Tianjin University,
92 Weijin Road, Tianjin 300072, China*



(Received 21 June 2022; accepted 7 December 2022; published 28 December 2022)

The effect of thermal shape fluctuations on the recurrent fluorescence of boron-cluster cations, B_N^+ ($N = 9-14$), has been investigated numerically, with a special emphasis on B_{13}^+ . For this cluster, the electronic structures of the ground state and the four lowest electronically excited states were calculated using time-dependent density-functional theory and sampled on molecular dynamics trajectories of the cluster calculated at an experimentally relevant excitation energy. The sampled optical transition matrix elements for B_{13}^+ allowed us to construct its emission spectrum from the thermally populated electronically excited states. The spectrum was found to be broad, reaching down to at least 0.85 eV. This contrasts strongly with the static picture, where the lowest electronic transition happens at 2.3 eV. The low-lying electronic excitations produce a strong increase in the rates of recurrent fluorescence, calculated to peak at $4.6 \times 10^4 \text{ s}^{-1}$, with a time average of $8 \times 10^3 \text{ s}^{-1}$. The average value is one order of magnitude higher than the static result, approaching the measured radiation rate. Similar results were found for the other cluster sizes. The results indicate that the effect makes a significant contribution to the radiative cooling, even given the exploratory nature of the study. Furthermore, the radiationless crossing between the ground-state and first-electronic-excited-state surfaces of B_{13}^+ was calculated, found to be very fast compared to experimental timescales, justifying the thermal population assumption.

DOI: [10.1103/PhysRevA.106.062826](https://doi.org/10.1103/PhysRevA.106.062826)

I. INTRODUCTION

Thermal radiation, long considered to be restricted to vibrational cooling, has also been demonstrated to occur from electronically excited states via the so-called recurrent fluorescence (RF) or Poincaré radiation. This type of radiation is attracting increasing attention as more and more molecules and clusters are recognized as emitters and in part also stimulated by the implications for astrophysics. To date, recurrent fluorescence has been observed in fullerenes [1,2], where the effect was first seen, in polycyclic aromatic hydrocarbon (PAH) molecules [3,4] and clusters of several metallic and semiconductor elements. For very recent results of direct astrophysical relevance, see Ref. [5]. Moreover, RF is known to be present in anionic, neutral, and cationic species, highlighting its general relevance at the nanoscale [6].

The existence of this type of radiation follows from time reversal once the presence of radiationless transitions is

established. Radiationless transitions connect different Born-Oppenheimer surfaces, allowing for the phenomenon of internal conversion (IC), in which electronic energy is converted into vibrational motion on the electronic ground state. Time reversal requires that the reverse process, i.e., inverse internal conversion (IIC), is also allowed, which means that in principle any excited electronic state that undergoes IC can be reached nonradiatively from the electronic ground state [7]. In RF, photon emission occurs from electronically excited states that are populated via IIC. As radiationless transitions are very well established for a number of molecules, the main concern about the presence of RF has been the question of to what degree molecular electronically excited states are populated thermally. The experimental evidence is now strongly in favor of the existence of RF, and the theoretical results here will add to this evidence.

Although RF was predicted several decades ago [8–10], photons emitted by this mechanism from mass-selected clusters and molecules were observed only recently for the molecules C_6^- [11], C_4^- [12] and naphthalene cations [13]. The vast majority of other studies of RF have deduced its presence from its quenching effect on the unimolecular

*tibor.holtzl@furukawaelectric.com

†hansen@lzu.edu.cn, Klavshansen@tju.edu.cn,
<http://www.klavshansen.cn/>

decays of the emitting particles (see Ref. [6] for a review of this method). The involved unimolecular signature decays can be the loss of atoms or larger fragments or, for anions and neutrals, thermal electron emission. The observed timescales for RF vary strongly with the system, from the highest rate constants found so far of 10^6 s^{-1} for cationic gold [14] and cobalt [15] clusters to close to the typical vibrational radiative timescales, which are four orders of magnitude longer.

Two of the three cases where RF photons have been detected directly from mass-selected molecular beams (C_6^- and C_4^-) employed a narrow detection window centered on the wavelengths where the particles in their ground-state absorb light [11,12]. The selective detection of this narrow spectral region was motivated by the desire to establish the origin of the photons. In the experiment measuring the spectrum of photons emitted from naphthalene, a significant broadening relative to the ground-state absorption spectrum was observed [13].

Such broadening is not unexpected and can be understood qualitatively as the consequence of the varying geometric structures sampled by the thermal excitation, with concomitant sampling of transition energies and oscillator strengths across the involved potential-energy surfaces. Spectral smearing is thus expected to be intrinsic to the RF phenomenon.

Measurements of the quenching effect of radiation on competing processes usually provide only a single value in the form of the photon emission rate constant. This value is the thermally averaged photon emission rate constant at the total excitation energy, where it equals the unimolecular decay rate constant, $k_{\text{ph}} \sim k_{\text{unimol}}$, because this relation defines the energy where the emission rate constant is measured (see Ref. [6] for a detailed explanation).

Electronically excited states characterized spectroscopically tend to misrepresent emission rate constants because these data usually pertain to only the very limited part of the configuration space that corresponds to excitation from a ground-state geometry. Pump-probe experiments explore a larger part of phase space, but the sampling is still limited to short and relatively localized trajectories in phase space. In contrast, highly excited and free-roaming species will explore much wider regions of configuration space. The effective thermally averaged transition energies and oscillator strengths will therefore, in general, differ from values derived from low-temperature spectroscopic data. Hence, the thermal exploration of potential-energy surfaces provides information about their shape. The investigation of this effect for well-characterized systems is the main motivation of this work.

The system chosen for this study is boron clusters, for which the effective (averaged) photon emission rate constants, but no emission spectra, have been measured upon laser excitation [16]. The experimentally measured radiation rate constants for these clusters are significant, reaching, for example, $6 \times 10^4 \text{ s}^{-1}$ for B_{13}^+ and $5 \times 10^5 \text{ s}^{-1}$ for B_9^+ . These high values strongly suggest that the emission mechanism is RF and indicate that the clusters possess optically active electronically excited states at low energies. In this work, most attention is given to B_{13}^+ , for which the ground-state geometry has been determined based on spectroscopic experiments [17]. We expect that the general picture revealed for this cluster applies equally well to other boron clusters

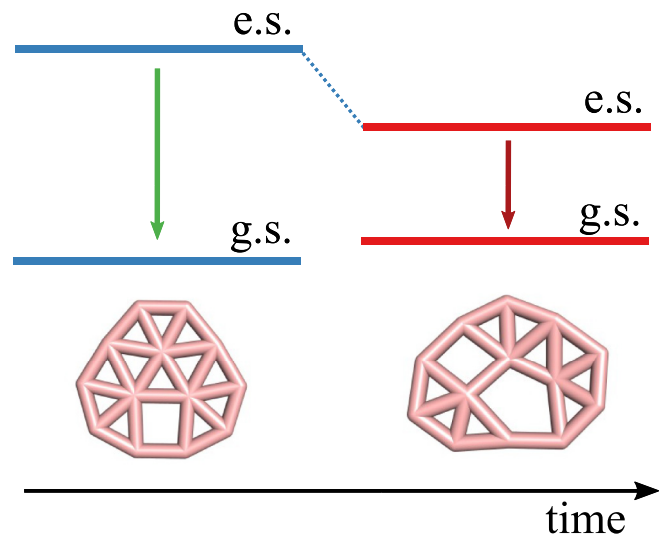


FIG. 1. Schematic illustration of the possible reduction of the energy difference between the ground state and the first excited state of a cluster, caused by temperature-induced geometrical deformations.

which, as noted in passing, by themselves are very interesting objects, with remarkable planar geometries, possessing fascinating fluxionality properties [17–21]. Moreover, low-lying quasidegenerate electronic states in boron clusters have also been shown to play an important role, as shown by electron wave-packet dynamics [22].

The theoretical work on the question presented here is exploratory in nature. Several approximations and some assumptions are needed to make any inroads into the problem. This should be made clear from the outset and will also be obvious at points in the text where approximations are needed. The results here are thus of a qualitative nature in spite of the application of advanced quantum-mechanical methods. The qualitative nature of the results notwithstanding, they still point to a very strong effect of thermal excitations on emission spectra, one which is most likely underestimated.

II. THERMAL SHAPE FLUCTUATIONS AND ELECTRONIC STRUCTURE

The central idea of this work is illustrated schematically in Fig. 1. For a cluster in its ground-state geometry with a large energy difference between the electronic ground state and the first electronic excited state (left part of Fig. 1), an optical transition between such states will translate into a small radiation rate [23]. This is not consistent with the observed high photon emission rate constants of, for example, laser-excited boron clusters [16]. However, the geometry of highly excited clusters will fluctuate over time, as illustrated schematically on the right side of Fig. 1. This dynamics can reduce the energy difference between the ground state and the electronically excited states. This will cause a higher thermal population of the excited states, which results in faster photon emission [6].

A calculation of the effect of this reduction of the excitation gap (electronic transitions modified by structural deformation) was already done for Al_{13}^- based on a spherical box potential

of finite depth undergoing a spheroidal distortion [24], albeit without specifically considering thermal radiation.

III. COMPUTATIONAL DETAILS

To investigate this thermal deformation-induced effect in boron clusters, we performed molecular dynamics (MD) simulations with potential energies calculated using density-functional theory (DFT). The MD simulations are standard integration of the Newtonian equations of motion. Specifically, the linear-response time-dependent DFT (LR-TDDFT) formalism was employed in order to compute the lowest-lying low-spin excitations in B_N^+ ($N = 9-14$) clusters. For B_{13}^+ four electronic excitations were calculated. Because of the long computation times required for these calculations, only two electronic excitations were computed for the other cluster sizes. The computations were performed using the long-range corrected version of the Becke, 3-parameter, Lee–Yang–Parr exchange-correlation functional (CAM-B3LYP) [25] in combination with a split valence polarization basis set (def2-SVP) the valence double-zeta, polarized def2-SVP basis set [26]. Detailed method verification is described in the Supplemental Material [27].

The ground-state geometry of B_{13}^+ was experimentally identified in Ref. [17]. The molecular dynamics simulations on the first excited low-spin potential-energy surface were performed with a microcanonical (NVE) ensemble, with initial coordinates of the lowest-energy structure on the ground-state potential-energy surface (vertical excited state) and with initial nuclear velocities selected from a canonical energy distribution.

The choice of using a temperature for a microcanonical simulation was made because the decay dynamics of the beam defines an effective, microcanonical temperature, and this temperature can be determined. The relation was suggested by Gspann [28] and developed by Klots [29,30]. It reads (with $k_B = 1$)

$$T = D(1/\ln(\omega_a t) + 1/2C_v). \quad (1)$$

The parameters in this expression are the evaporative activation energy D , the frequency factor of the unimolecular rate constant ω_a , the experimental measurement time t , and the cluster's heat capacity C_v , given in units of Boltzmann's constant. In experiments where the suppression of the unimolecular decay is used as the signature of radiative decay, as is the case here, we can make the identification of the experimental timescale in Eq. (1) as $t = 1/k_p$. This is the time at which the thermal photon emission rate constant is equal to the unimolecular fragmentation rate constant, and the experimental time is therefore defined by this value. In brief, at higher excitation energies, instantaneous fragmentation is the dominant cooling channel, whereas at lower values, fragmentation is exponentially suppressed. Hence,

$$T = D[1/\ln(\omega_a/k_p) + 1/2C_v], \quad (2)$$

and this is therefore the energy at which the photon emission rate constant is determined experimentally.

For completeness we should mention that this temperature is the microcanonical value, but the difference from the canonical temperature can be ignored here. For more details

on this the reader can consult [23], and Ref. [31] discusses the meaning of the microcanonical temperature.

The value found for B_{13}^+ is 3900 K. In energy units this temperature is 0.33 eV. This temperature together with the speeds selected at random from the Maxwell-Boltzmann distribution give a total nuclear kinetic energy of 5.61 eV, close to the canonical average value of 5.48 eV. The simulations were started from the ground-state geometry and the first excited state. The energy of that state, 2.27 eV, should be added to the total energy.

The potential-energy surface of B_{13}^+ and the possible emission routes were explored using adiabatic molecular dynamics simulations of the S_1 state. The MD simulations propagate the system in time by solving the classical equations of motion for the nuclei while calculating the potential energy on all surfaces point by point with the DFT calculations mentioned above. The S_1 surface was chosen as a representative of an emitting surface, but the specific choice is not critical for the exploration of the phase space. The simulations were tested with two different time steps, 0.02 and 0.1 fs. The results were very similar, and longer simulations were therefore conducted with the latter value.

The small S_0 - S_1 energy differences that are calculated (see Sec. III) imply that nonadiabaticity is important. An accurate description of such effects is computationally demanding, and nonadiabatic effects are therefore explored only for B_{13}^+ . Detailed results are available in the Supplemental Material, while those using the spin-flip density-functional theory computations are shown in Fig. 3 below.

These computations make it possible to estimate the transition rate through the minimum-energy crossing points toward the S_0 and S_1 states. The magnitude of these time constants indicates that on the much longer microsecond experimental timescale the excited states can reach thermal populations. This allows us to sample the phase space using molecular dynamics simulations and estimate the radiative emission rate from the thermal populations of the excited states.

Computation of nonadiabatic couplings is described in the Supplemental Material.

IV. DYNAMICS OF ELECTRONIC EXCITED STATES

The top panel of Fig. 2(a) shows the energies of the four lowest electronic states, as well as the S_0 ground state, along the molecular dynamics trajectory for B_{13}^+ . The bottom panel presents the energies of the excited electronic states relative to the energy of S_0 . Interestingly, the four excited states and the ground state show a correlated pattern with time. As seen in Fig. 2(a), the energy difference between the first excited state and the ground state (red curve) at the initial configuration, and thus the lowest vertical excitation energy in the ground-state geometry, is over 2 eV. This energy difference reduces to below 1 eV at several later moments, showing the possibility of emission of lower-energy photons. Whether this possibility is realized depends on whether the states are thermally populated, which in turn depends on the excited-state energy relative to the ground-state energy and not on their difference with respect to the simultaneous energy of S_0 .

Geometry optimization starting from regions with a small S_0 - S_1 energy difference confirmed the existence of a structural

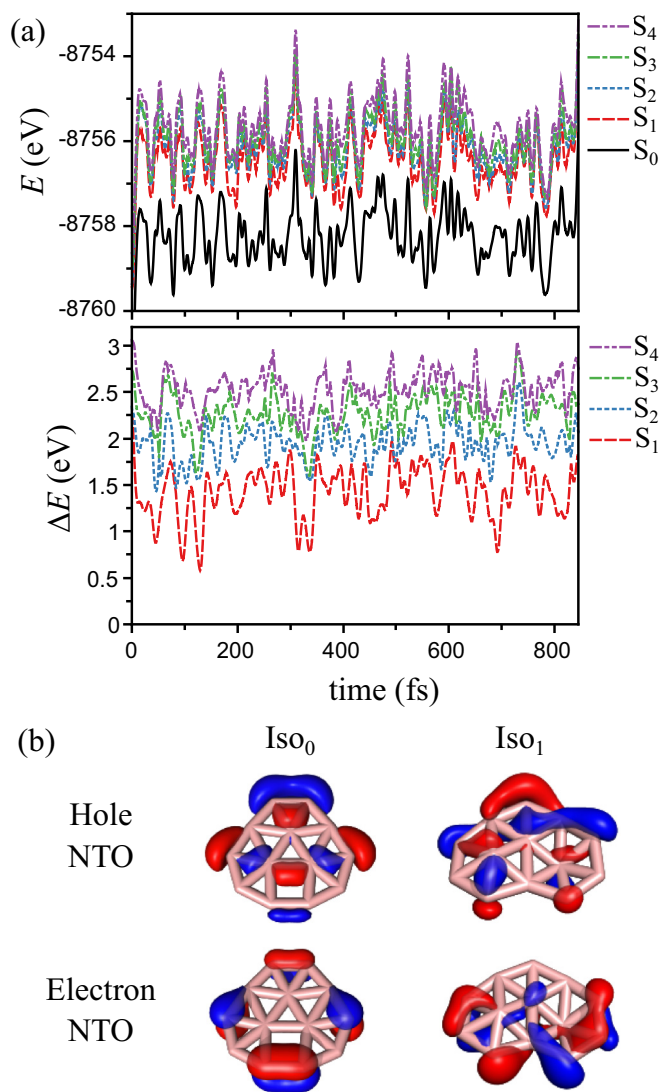


FIG. 2. (a) Top: Energies of the electronic excited states S_i ($i = 1-4$) and the ground state S_0 of B_{13}^+ as a function of simulation time. Bottom: Energy difference between each electronic excited state and the ground state. (b) Cluster geometries and the isosurfaces (isovalues: 0.05) of the leading natural transition orbital (NTO) pairs for the S_0 ground state at the lowest-energy geometry (initial structure, Iso_0 , at $t = 0$) and at a low-energy structural isomer (Iso_1 at an optimized intermediate structure; see Fig. 3).

isomer with an energy which is only slightly higher than the lowest-energy isomer, as shown in Fig. 2(b). In both cases, the excitation from the ground to the first excited state can be described approximately by a single-electron configuration, which involves the formal electron transfer from the highest occupied molecular orbital (HOMO) to the lowest unoccupied molecular orbital (LUMO). This is accurately reflected by the fact that the excitation can be well described using a single natural transition orbital (NTO) pair, where the shape of the hole and the electron NTOs resemble those of the HOMO and LUMO, respectively. It is clearly visible that the shapes of the electron and hole NTOs follow the distortion of the cluster shapes towards the low-energy structural isomer.

The analysis shown so far involves the adiabatic approximation; that is, the MD trajectory was propagated on a single potential-energy surface, with the different surfaces computed independently. However, it has been shown that the dynamics of boron clusters also involves nonadiabatic effects [22], including the presence of several conical intersections and avoided crossings. Crossing regions of the potential-energy surface play a pivotal role in internal conversion and will, through time reversal, likewise play a role for IIC. Conical intersections were therefore investigated in more detail.

V. NONADIABATIC EFFECTS

The relevance of excited states in the description of the radiative cooling of a cluster or molecule is, to some degree, a question of timescales. States need to be populated. To assess whether excited states are populated, the timescale determined by the coupling between them should be compared with the microsecond or longer experimental timescale at which the populations are monitored, i.e., the time at which the radiative cooling is measured. This long timescale puts very mild conditions on the coupling.

In this section we explore a part of the potential-energy surface at which the relative populations of the Born-Oppenheimer states are calculated by calculating nonadiabatic couplings. As the typical timescale of RF cannot be attained using conventional molecular dynamics simulations, we explore the stationary (zero-derivative) points and the crossing points between the lowest two singlet states in the neighborhood of the lowest-energy geometry. The crossing points on the computed trajectories (described in the caption of Fig. 3) clearly show the possibility of nonradiative transitions between the two lowest singlet states. Crossings between higher excited states should also be present, but they do not alter the results found here for the two lowest states fundamentally.

The small energy difference between the S_0 and S_1 states of B_{13}^+ will induce large nonadiabatic couplings and also generate conical intersections. Here, we have optimized the initial and isomeric geometries of B_{13}^+ and systematically explored the two adjacent minimum-energy crossing points (MECPs; Fig. 3). The MECPs are the lowest-energy points on the line defining the intersection of the two surfaces. The variations in potential energies are much smaller than the energy used in the MD simulations. Hence, the crossing configurations shown are well within energetic reach. The computations were performed using spin-flip time-dependent density functional theory (SF-TDDFT), which was motivated by the fact that unlike the conventional TDDFT, this method correctly describes the topology of the conical intersections involving the S_0 state [32]. To further assess the accuracy of our computations, we recomputed the geometries and energies of the minima and the MECPs using spin-flip equation of motion coupled-cluster singles and doubles (SF-EOM-CCSD) and extended complete active space second order perturbation theory (XMS-CASPT2) methods (see Table S1 in the Supplemental Material).

To illustrate the topology of the S_0 and S_1 potential-energy surfaces we computed the linear synchronous transit paths (i.e., linear interpolation in Cartesian coordinates) between the minima and the MECPs shown in Fig. 3(b). The abscissa

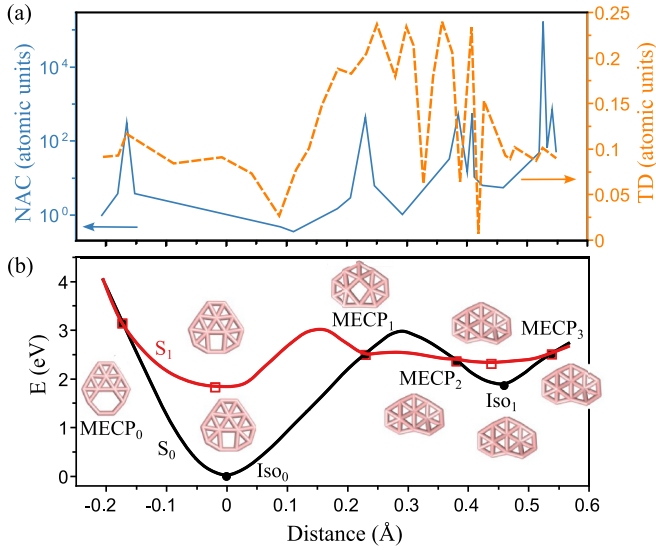


FIG. 3. (a) Magnitude of the transition dipole moments (TD) and the nonadiabatic coupling vectors (NAC, logarithmic scale), both in atomic units (hartrees/ a_0 for NAC) along the constructed linear synchronous interpolation curve described in the main text. The abscissa is the rms of the stretched nuclear coordinates. (b) Geometries and energies along the path between the lowest-energy Iso₀ and intermediate Iso₁ geometries and the adjacent minimum-energy crossing points of the two lowest potential surfaces (S_0 and S_1). Stationary and minimum-energy crossing points are indicated by dots. The paths from the isomer Iso₀ to MECP₀ and from Iso₁ to MECP₃ are stretched for visibility. Calculations are performed using spin-flip Density Functional Theory, employing the Becke half&half functional, containing 50% Hartree-Fock exchange, and the def2-SVP basiset (SF-BH&HLYP/def2-SVP). The S_0 - S_1 excitation energy at zero abscissa differs from the previously quoted 0.225 and 0.227 eV because the value here is not vertical; that is, the S_0 and S_1 geometries are different, except in the case of the MECPs.

in both curves is the rms deviation of the atomic positions compared to Iso₀. Note that Fig. 3(b) is not a trace of the MD simulation and that the data do not enter the statistics derived from that simulation. Figure 3 shows that there are several MECPs between the S_0 and S_1 potential-energy surfaces on this curve. The energies of those two states at the isomeric structures are not much higher than the ground-state energy in the lowest-energy minimum and will thus be easily accessible under the experimental conditions of radiative-cooling studies of excited clusters in molecular beams, as discussed above. This is confirmed by calculations of the rate coefficients for crossing, which involve thermally activated reactions (see the Supplemental Material for details).

The magnitude of the transition dipole moment between the S_0 and S_1 states determines the rate of photon emission via the electronic transition between the two states, while the magnitude of the nonadiabatic coupling indicates the efficiency of the nonradiative relaxation and the excitation. It is clearly seen from Fig. 3 that, as expected, the probability of the nonradiative relaxation or excitation is very high in the vicinity of the MECPs, as the magnitude of the nonadiabatic couplings increases by factors of $\sim 10^2$ to 10^4 compared to the original value, while the magnitude of the transition dipole

moment increases by a more modest factor of 2–3. Hence, although photon emission is more probable near MECPs and the conical intersections that may be present than elsewhere, the nonradiative coupling is much more enhanced at these points. In this connection it is worth noting that nonadiabatic wave-function dynamics of boron clusters have indicated the presence of several conical intersections and frequently occurring high nonadiabatic couplings [22]. Transition-state-theory calculations (see the Supplemental Material for more details) show that the transition rate at MECP₁ is approximately $4 \times 10^9 \text{ s}^{-1}$ and thus well within the microsecond timescale of the emission. These results showing a rapid exchange of energy between the electronic ground state and the first excited state of B_{13}^+ strongly support the suggestion that photon emission in boron clusters proceeds via IIC and recurrent fluorescence in boron-cluster cations.

VI. MICROCANONICAL AVERAGING

The combination of time-dependent energies of the electronic state S_0 ($i = 0-4$) energies with the oscillator strengths f_i for the transitions allows the construction of the emission spectrum of B_{13}^+ for the sampled geometries. In the rapid-equilibration scheme relevant here the statistical weight of an excited state is given by the level density of the kinetic energy for that geometry. With E being the total (conserved) excitation energy relative to the absolute ground state and $V_i(x)$ being the potential energy of state i ($i = 0-4$) in the geometry labeled by x , the un-normalized populations of the states g_i are, with $s \equiv 3N - 6$, equal to

$$g_i(x) = c[E - V_i(x)]^{s/2-1}, \quad i = 0, 1, \dots \quad (3)$$

This expression is simply the density of states for s momenta with a total energy $E - V_i(x)$ and the sampled geometry in the simulated microcanonical ensemble. The assumption is the fundamental postulate of thermodynamics that all quantum states are populated with equal probability. The constant c is identical for the different states, as is the number of degrees of freedom, s , of the nuclear motion. The population of the state i is therefore

$$p_i = \frac{g_i(x)}{\sum_j g_j(x)}, \quad (4)$$

where j runs over all relevant states. For values of $V_i(x)$ exceeding E , obviously, state i is unpopulated. This expression for the population should be understood in the same way as the spectrum of geometries sampled in the MD calculation. Both are classical results, and as such they do not describe the motion of the system and the associated time-dependent state populations. Rather, both geometries and populations represent a more or less complete sampling of the properties of the system when it is allowed to propagate for an extended period of time.

With the oscillator strengths and energies of the surfaces the rates of photon emission can thus be computed as a function of time along the trajectory. At each point the photon emission rate constant from state i ($i = 1-4$) is given by [23]

$$k_p^i = 7.421 \times 10^{-22} \text{ Hz } f_i v_0^2 p_i. \quad (5)$$

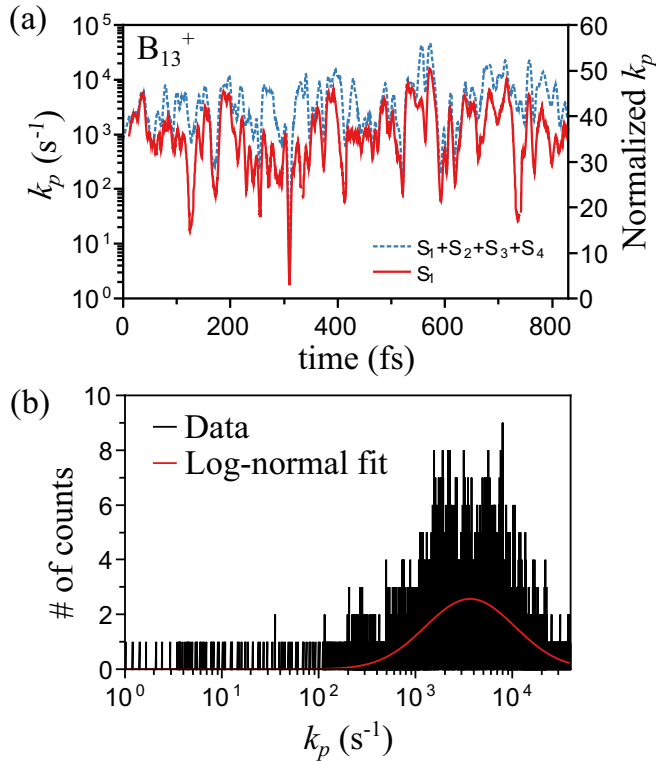


FIG. 4. (a) Time-dependent radiation rate constant calculated for B_{13}^+ at an initial kinetic energy corresponding to a temperature of 3900 K. The red lower curve shows the radiation constant when only emission from S_1 is considered. The blue upper curve gives the emission rate constant for the first four excited states. Note that these curves are used for the purpose of sampling representative parts of phase space and not to follow the system to experimental timescales. (b) Distribution of k_p for B_{13}^+ as derived from the time-dependent behavior in (a). A log-normal distribution is used to fit an average k_p value.

In this expression, f is the oscillator strength, and $h\nu_0$ is the transition energy. For B_{13}^+ the total rate constant is then calculated as the sum of the four k_p^i values [see Fig. 2(a)]. For the other cluster sizes two electronic excited states were computed.

VII. EMISSION SPECTRA

The result for B_{13}^+ is presented in Fig. 4(a), where the total radiation rate constant is shown as a function of MD simulation time. Figure 4(a) also shows the effect of the number of excited states included in the calculation. The values vary strongly with time, as expected from the pronounced dependence of the energy of the excited states seen in Fig. 2. The rate constant reaches significantly higher values than for the static picture in the ground-state geometry, as highlighted by the scale on the right-hand axis, where k_p is normalized with respect to the rate at 0 K.

Another important observation from this result is the quite high absolute values that are reached along the simulation (axis on the left), peaking at $4.6 \times 10^4 \text{ s}^{-1}$. This value is very close to the experimental result in Ref. [16], which is $(6.1 \pm 2.8) \times 10^4 \text{ s}^{-1}$. In Fig. 4(b), the distribution of k_p values is depicted and fitted by a log-normal distribution. This allows

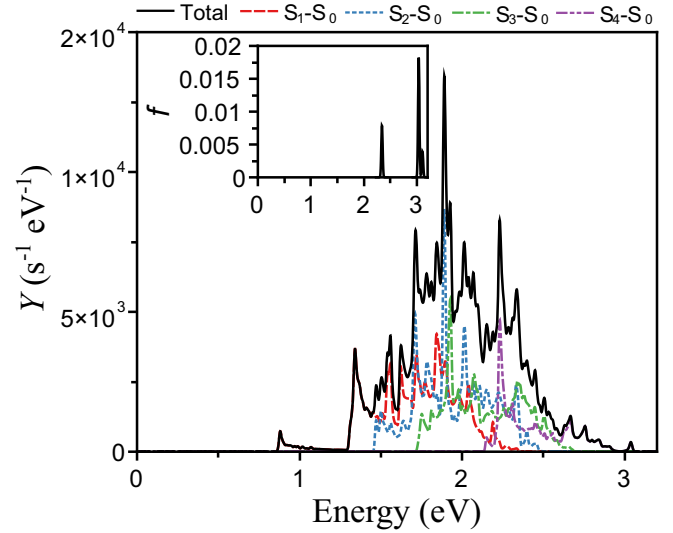


FIG. 5. Emission spectrum of B_{13}^+ at the microcanonical temperature of 3900 K. The spectrum is calculated with the difference in energy of the electronic states to the absolute ground state, yielding the populations of the excited states and the oscillator strengths of those transitions. The sum $\sum_i Y_i$ is shown as a black line. The static emission spectrum, calculated with LR-TDDFT on the ground-state geometry of the cluster, is shown in the inset. It is constructed by assuming Gaussian functions around each transition, with an artificial width of 0.05 eV.

an estimation of the average k_p , yielding the value $8 \times 10^3 \text{ s}^{-1}$. As discussed below, this improved estimate is still most likely an underestimate of the values that are generated by the RF mechanism.

Based on the energies and oscillator strengths calculated for the four electronic states of B_{13}^+ , an emission spectrum is constructed, as presented in Fig. 5. The spectrum is calculated as the sum over the spectra produced by emission from the four excited states, with the expression for each of them equal to

$$Y_i(h\nu) = \frac{\sum_j' k_{i,j}}{\Delta h\nu N}, \quad (6)$$

where N is the total number of sampled points and the primed sum over j is over the points where the photon energy is found in the interval between $h\nu$ and $h\nu + \Delta h\nu$. The total spectrum is then

$$Y(h\nu) = \sum_i Y_i(h\nu). \quad (7)$$

It shows bands of significant widths for each of the excited states, spanning between 0.85 and 3 eV. Note that the lower energy of 0.85 eV is the value observed in the relatively short simulations. The true lower limit is most likely much lower, approaching close to zero (see Fig. 3).

This high-temperature spectrum is very different from the static picture calculated with LR-TDDFT at the ground-state geometry (shown in the inset). That spectrum is composed of a small set of discrete transitions, with the first occurring at 2.27 eV. It is worth reiterating that the spectrum in Fig. 5 represents the configurations encountered in the

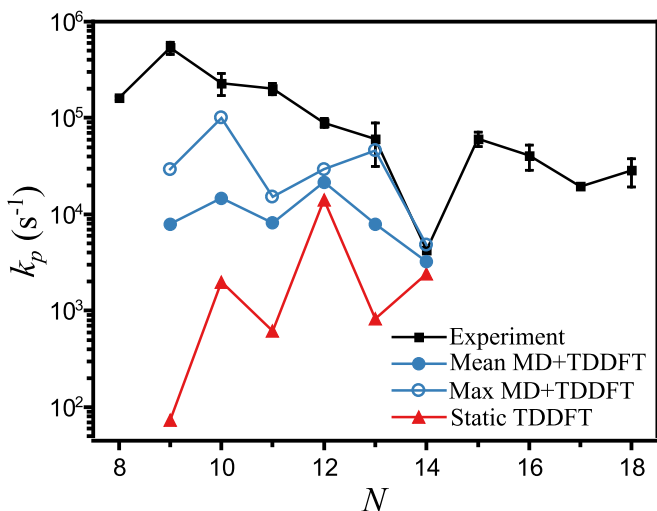


FIG. 6. Radiation rate constants of B_N^+ clusters calculated with the MD+TDDFT analysis (blue circles). Solid and open circles correspond to the mean and maximum values, respectively. For comparison, the experimental data from Ref. [16] are reproduced (black squares), together with a calculation using TDDFT on the ground-state geometries (red triangles).

MD simulation. The true lower-energy cutoff will be lower, as demonstrated by the level crossings seen in Fig. 3. The time-average, energy-integrated total oscillator strength at the elevated temperature shown in Fig. 5 is lower than the static values, but not significantly so.

The analysis performed for B_{13}^+ was also conducted for the boron clusters with sizes $N = 9-12, 14$. The results for these clusters are included in the summary of all the radiative rate constants shown in Fig. 6. This figure compares the MD time-average rates obtained from the computations in this work with the experimental data of Ref. [16]. Additionally, the maximal values are presented as well as the rates calculated using LR-TDDFT on the (static) ground-state geometries. These were obtained from Ref. [18] and were reoptimized at the CAM-B3LYP/def2-SVP level.

Although not all the size-dependent trends of the experimental data are reproduced by the MD+TDDFT simulations, the improvement relative to the static geometries is significant. The improvements for sizes 9, 10, 11, and 13, in particular, are considerable. For B_{13}^+ , all four states contribute with a similar magnitude to the total emission rate constant. We therefore expect that the restriction to a limited number of excited states is responsible for part of the remaining discrepancy between experiment and theory, in addition to the role of nonadiabatic effects, which were not included in this calculation but are known to be relevant, as discussed in Sec. V. These are, briefly, the uncertainty of the frequencies (described briefly in the Supplemental Material) and the accuracy of the computation (SF-DFT and the more accurate XMS-CASPT2). In addition, the branching ratio onto the two curves at the MECP is associated with large uncertainties. Yet another missing component is the neglect of transitions between excited states in the calculations. Such transitions are not simple to estimate, but it is clear that their presence will increase the emission rate constant. The effect on the spectra is less certain, but most likely, they will add intensity on the red side.

We cannot rule out that a longer MD run will also contribute higher-intensity parts of the phase space, given the approximate log-normal shape of the k_p distribution. This distribution suggests a long tail toward high values.

VIII. SUMMARY AND PERSPECTIVES

In this work, the role of temperature in the radiative cooling of boron clusters was investigated by means of molecular dynamics simulations in combination with time-dependent density-functional theory and high-level *ab initio* computations. With a focus on the computational analysis of the B_{13}^+ cluster, it was shown that at the effective temperature of 3900 K, estimated from experimental parameters, geometry fluctuations cause significant changes in the electronic structure of the cluster. At several points in the explored geometry, the energy of the low-lying electronic excited states is reduced by a significant amount, with a concomitant exponential increase in the recurrent fluorescence radiation rate. Moreover, the possibility that energy is transferred nonradiatively via IC and IIC was explicitly demonstrated by large nonadiabatic coupling vectors when the electronic ground and first electronic excited states cross.

The thermal effects have two important consequences. One is that the rates estimated in this work reduce the discrepancy between theory and experiment significantly, giving a strong indication of the importance of the effect and the modification of the RF values relative to ground-state properties.

The second consequence is the occurrence of a significant broadening and redshift of the emission spectrum relative to that of the ground state. The redshift seen in the thermalized spectrum must also be expected to be a general occurrence. The lowest-energy geometries tend to be those that maximize the HOMO-LUMO gap for molecules and clusters, and thermal excitation tends to reduce this gap and generally reduce the excited-state energies. The tendency is amplified in the emission spectra by the fact that low-energy states tend to be more populated by simple phase-space arguments. Hence, this effect will also favor a redshift of the spectrum.

There is, therefore, every reason to believe that the thermal effects on the emission rate constants and on the spectral shapes described here will both be present in other systems that dissipate energy by recurrent fluorescence. It should also be noted that the deformations explored in Fig. 3 imply that emitted photons will have energies reaching down to close to zero due to level crossings. Measured spectra will therefore show the effect even more strongly than calculated here.

The internal excitation energy was determined as the sum of kinetic energies sampled from the canonical ensemble with the added energy of the S_1 state in the ground-state geometry. The choice of using the S_1 state and not the electronic ground state as the initial configuration compensates for the fact that a fraction of the clusters are in electronically excited states, both S_1 and the higher states, and that this excitation energy should be added to the nuclear kinetic energy of 5.61 eV.

It also compensates for the fact that the deformed clusters, which take up most of the phase space, will have nuclear potential energies above those of the harmonic motion of the ground state. It is not possible to know the precise value of

this contribution before the entire phase space is sampled or the caloric curve is determined experimentally, but an estimate can be obtained by considering the melting enthalpy. The bulk melting point is 2349 K, which is below the temperature here, suggesting that the clusters are liquid or in the equivalent finite-size-particle phase. The melting enthalpy for bulk is 0.52 eV per atom for bulk. Adding this would more than double the excitation energy. The thermal estimates calculated here are therefore of a very conservative nature, which should be kept in mind when comparing them to the experimental values.

Measurement of recurrent fluorescence spectra is a field in its infancy, with only one spectrum reported so far [13]. The measurements of the spectrum of emitted photons by hot naphthalene molecules in Ref. [13] show a spectrum which is significantly broadened compared to the ground-state absorption case. This experimental observation agrees qualitatively with our calculations in Fig. 5.

Measurements of thermal emission spectra of highly excited clusters provide a method to explore the potential-energy surfaces of molecules and clusters, which presently cannot be done with other methods, such as traditional spectroscopy. The results calculated here suggest that such measurements

will have significant effects compared to ground-state geometry spectra and emission rate constants. It should be emphasized that the limitations in the computational protocols applied in this work, unavoidable at the present stage of theory, will impose limitations on the accuracy of the numerical results derived. As argued, we expect that refinements of the method to calculate the consequences of the phenomenon will give even higher photon emission rates. The ultimate information will be provided by experiments. The results here tell us that these experiments are worth performing.

ACKNOWLEDGMENTS

This work is supported by the Research Foundation Flanders (FWO, Grant No. G.OA05.19N) and the KU Leuven Research Council (Project No. C14/22/103). P.F. acknowledges the FWO for a senior postdoctoral grant. K.H. acknowledges support from the National Science Foundation of China under NSFC Grant No. 12047501 and the Ministry of Science and Technology of the People's Republic of China for the 111 Project under Grant No. B20063. T.H. is grateful for the János Bolyai Research Scholarship of the Hungarian Academy of Sciences (Grant No. BO/00642/21/7).

-
- [1] K. Hansen and E. Campbell, *J. Chem. Phys.* **104**, 5012 (1996).
- [2] J. U. Andersen, C. Brink, P. Hvelplund, M. O. Larsson, B. Bech Nielsen, and H. Shen, *Phys. Rev. Lett.* **77**, 3991 (1996).
- [3] S. Martin, J. Bernard, R. Brédy, B. Concina, C. Joblin, M. Ji, C. Ortega, and L. Chen, *Phys. Rev. Lett.* **110**, 063003 (2013).
- [4] J. Bernard, A. Al-Mogeeth, A.-R. Allouche, L. Chen, G. Montagne, and S. Martin, *J. Chem. Phys.* **150**, 054303 (2019).
- [5] S. Iida, W. Hu, R. Zhang, P. Ferrari, K. Masuhara, H. Tanuma, H. Shiromaru, T. Azuma, and K. Hansen, *Mon. Not. R. Astron. Soc.* **514**, 844 (2022).
- [6] P. Ferrari, E. Janssens, P. Lievens, and K. Hansen, *Int. Rev. Phys. Chem.* **38**, 405 (2019).
- [7] V. Chernyy, R. Logemann, J. Bakker, and A. Kirilyuk, *J. Chem. Phys.* **145**, 024313 (2016).
- [8] A. Nitzan and J. Jortner, *J. Chem. Phys.* **56**, 5200 (1972).
- [9] A. Nitzan and J. Jortner, *J. Chem. Phys.* **71**, 3524 (1979).
- [10] S. Leach, in *Polycyclic Aromatic Hydrocarbons and Astrophysics*, edited by A. Léger, L. d'Hendecourt, and N. Boccara, NATO Advanced Studies Institute, Series C: Mathematical and Physical Sciences (Springer, Dordrecht, 1987), Vol. 191, pp. 99–127.
- [11] Y. Ebara, T. Furukawa, J. Matsumoto, H. Tanuma, T. Azuma, H. Shiromaru, and K. Hansen, *Phys. Rev. Lett.* **117**, 133004 (2016).
- [12] M. Yoshida, T. Furukawa, J. Matsumoto, H. Tanuma, T. Azuma, H. Shiromaru, and K. Hansen, *J. Phys.: Conf. Ser.* **875**, 012017 (2017).
- [13] M. Saito, H. Kubota, K. Yamasa, K. Suzuki, T. Majima, and H. Tsuchida, *Phys. Rev. A* **102**, 012820 (2020).
- [14] K. Hansen, P. Ferrari, E. Janssens, and P. Lievens, *Phys. Rev. A* **96**, 022511 (2017).
- [15] K. Peeters, E. Janssens, K. Hansen, P. Lievens, and P. Ferrari, *Phys. Rev. Res.* **3**, 033225 (2021).
- [16] P. Ferrari, J. Vanbuel, K. Hansen, P. Lievens, E. Janssens, and A. Fielicke, *Phys. Rev. A* **98**, 012501 (2018).
- [17] M. R. Fagiani, X. Song, P. Petkov, S. Debnath, S. Gewinner, W. Schöllkopf, T. Heine, A. Fielicke, and K. R. Asmis, *Angew. Chem., Int. Ed.* **56**, 501 (2017).
- [18] E. Oger, N. R. Crawford, R. Kelting, P. Weis, M. M. Kappes, and R. Ahlrichs, *Angew. Chem., Int. Ed.* **46**, 8503 (2007).
- [19] H.-J. Zhai, Y.-F. Zhao, W.-L. Li, Q. Chen, H. Bai, H.-S. Hu, Z. A. Piazza, W.-J. Tian, H.-G. Lu, Y.-B. Wu, G.-F. Wei, Z.-P. Liu, J. Li, S.-D. Li, and L.-S. Wang, *Nat. Chem.* **6**, 727 (2014).
- [20] B. Kiran, G. Gopa Kumar, M. T. Nguyen, A. K. Kandalam, and P. Jena, *Inorg. Chem.* **48**, 9965 (2009).
- [21] W.-L. Li, X. Chen, T. Jian, T.-T. Chen, J. Li, and L.-S. Wang, *Nat. Rev. Chem.* **1**, 0071 (2017).
- [22] Y. Arasaki and K. Takatsuka, *J. Chem. Phys.* **150**, 114101 (2019).
- [23] K. Hansen, *Statistical Physics of Nanoparticles in the Gas Phase* (Springer, Dordrecht, 2018).
- [24] V. V. Kresin and Y. N. Ovchinnikov, *Phys. Rev. B* **73**, 115412 (2006).
- [25] T. Yanai, D. P. Tew, and N. C. Handy, *Chem. Phys. Lett.* **393**, 51 (2004).
- [26] F. Weigend and R. Ahlrichs, *Phys. Chem. Chem. Phys.* **7**, 3297 (2005).
- [27] See Supplemental Material at <http://link.aps.org/supplemental/10.1103/PhysRevA.106.062826> for an estimation of transition rates through the MECPs, a verification of the computational method, and information about the computational approach for strong correlation and nonadiabatic effects.
- [28] J. Gspann, in *Physics of Electronic and Atomic Collisions*, edited by S. Datz (North Holland Press, Amsterdam, 1982), pp. 79–96.
- [29] C. E. Klots, *Nature (London)* **327**, 222 (1987).
- [30] C. E. Klots, *Z. Phys. D* **21**, 335 (1991).
- [31] J. U. Andersen, E. Bonderup, and K. Hansen, *J. Chem. Phys.* **114**, 6518 (2001).
- [32] B. G. Levine, C. Ko, J. Quenneville, and T. J. Martínez, *Mol. Phys.* **104**, 1039 (2006).